



Corrosion resistance of austenitic stainless steel welds with no-backing gas

Jeremy McNicol¹ · Badri Narayanan² · Narasi Sridhar¹ · Carolin Fink¹

Received: 27 September 2022 / Accepted: 8 December 2022 / Published online: 14 December 2022
© International Institute of Welding 2022

Abstract

Stainless steel pipe welds for service applications in corrosive environments typically use gas tungsten arc welding (GTAW) and require the use of an inert backing gas in order to minimize or prevent root bead contamination and oxidation. This adds significant cost and complexity to the welding of stainless steel pipe due to access restrictions, personnel safety, and/or economic factors. In this work, waveform-controlled gas metal arc welding (GMAW) was used for no-backing gas (NBG) welding of Type 304L austenitic stainless steel. Pitting corrosion behavior locally in the backside heat-affected zone and root bead weld metal was characterized using a syringe cell setup for cyclic potentiodynamic polarization (CPP) measurements. The CPP results indicate that the NBG welds have a similar pitting corrosion resistance as compared to reference GTAW and GMAW welds made with pure argon purging and an argon-oxygen mixture backing gas. The repassivation potential of the NBG welds was comparable to the reference welds, while the pitting potential was slightly lower. Weld bead appearance, weld metal ferrite, and heat tint oxidation were also characterized, and discussed with regard to the observed pitting corrosion resistance.

Keywords Gas metal arc welding · No-backing gas welding · Stainless steel · Pitting corrosion

1 Introduction

Gas tungsten arc welding (GTAW) is typically employed for open-gap root pass welding of stainless steel piping. The GTAW process uses an inert backing gas (usually argon or argon-helium mixtures) to minimize or eliminate oxidation near the weld root on the inside diameter of the pipe. However, the use of backing gas adds significant complexity and cost to pipe fabrication, and poses a considerable safety hazard (asphyxiation) [1]. Alternative welding techniques utilizing advanced or modified short-arc gas metal arc welding (GMAW) processes without backing gas have been proposed many years ago [2], but are still not widely adapted, in particular for service applications in corrosive environments.

Approximately 20 years ago, Messer et al. [2] first combined an inverter power source, silicon-rich filler wire, and tri-mix shielding gas (helium-argon-carbon dioxide) at an increased flow rate for no-backing gas (NBG) welding of Type 304/304L and 316/316L austenitic stainless steel pipe. Minor oxidation and discoloration at the root pass inner surface were reported. However, no significant differences in corrosion behavior and mechanical properties were observed when compared to control welds with argon backing [2]. The GMAW NBG process was later applied to heavy wall Type 321/347 stainless steel [3] and 9Cr-1Mo-V steel (P91) welds [4] with code-acceptable results. Advanced or modified short-arc GMAW processes without backing gas have since been successfully used for stainless steel pipe welding in power, oil and gas, and liquid nitrogen gas industries [1]. However, despite the gain in safety and productivity, widespread use of the technology faces many obstacles, as discussed by Chiluvuri et al. [1]. In recent years, further improvements in GMAW waveform technology as well as the continuing high numbers of asphyxiation-related fatalities have sparked renewed interest in NBG welding techniques [1, 5].

Limited information is available in the open literature on the achievable quality and service performance of stainless

Recommended for publication by Commission II—Arc Welding and Filler Metals.

✉ Carolin Fink
fink.242@osu.edu

¹ Department of Materials Science and Engineering, The Ohio State University, Columbus, OH, USA

² The Lincoln Electric Company, Euclid, OH, USA

steel no-backing gas (NBG) welds particularly in corrosive environments. In this study, Type 304L stainless steel welds were made using matching ER308LSi and ER308L filler wires in an open-gap joint configuration without the use of backing gas. Advanced/modified short-circuit GMAW was used for the root pass weld. An additional hot pass was placed using pulsed GMAW. Visual inspection, metallographic characterization, and corrosion testing were performed. Previous work using standard immersion testing according to ASTM G48 Method A (immersion pitting test in 6 wt% FeCl₃) [6] had shown no significant difference in corrosion weight loss between the GMAW NBG welds and reference GTAW welds with argon backing [5]. Some pitting corrosion had been observed in the root beads and in the base metal away from the weld on the backside surface of the NBG welded samples (i.e., representing the as-welded inner surface of a pipe weld). Consequently, in this study, a corrosion test technique was applied that enabled determination of corrosion resistance locally in different regions on the backside surface of the weld. Using an electrochemical syringe cell setup [7], cyclic potentiodynamic polarization (CPP) curves were obtained from the backside heat-affected zone and root bead weld metal. Results were compared to curves obtained from GMAW welds made with pure argon backing gas, GMAW welds with an argon/oxygen mixture as backing gas, and from a GTAW reference weld with argon backing. In addition, weld bead appearance, weld metal ferrite, and heat tint oxidation were characterized, and discussed with regard to the observed pitting corrosion resistance.

2 Experimental procedures

2.1 Materials and weld preparation

The base and filler metals used in the present study are commercial Type 304L stainless steel and matching filler wires ER308L and ER308LSi. Compositions are provided in Table 1. The base metal thickness was 9.5 mm (3/8 in.) and the wire diameter was 0.9 mm (0.035 in.). The joint geometry is shown in Fig. 1. Six 203-mm (8 in.)-long welds were prepared using a modified short-arc GMAW process (SC-GMAW) for welding the root pass. Then, a pulsed GMAW (GMAW-P) process was used to weld a hot pass over half of the weld length, i.e., 101 mm (4 in.). Welds were created at a 50° angle for the root pass and a 10° angle for the hot pass to simulate pipe welding in the horizontally rotated (1G) position. The shielding gas mixture used for all welds was a helium tri-mix of 90% He, 7.5% Ar, and 2.5% CO₂. Along with no-backing gas (NBG) welds, two different backing gas combinations were studied: 100% Ar and a mixture of 95% Ar and 5% O₂ in order to vary the amount of oxygen present on the weld backside. Table 2 gives an overview of all test welds. The welding parameters and conditions are summarized in Table 3.

2.2 Light optical and electron microscopy

Weld cross sections were machined for metallographic analysis from each weld, i.e., from both the SC-GMAW root

Table 1 Chemical composition (wt%) of base and filler metals

Material	C	Cr	Ni	Mo	Mn	Si	P	S	N	Cu	Others
304L	0.02	18.1	8.0	0.28	1.65	0.31	0.026	0.026	0.076	0.48	0.23
ER308L*	0.01	19.7	9.7	0.17	1.7	0.37	0.02	0.01	0.0	0.18	–
ER308LSi*	0.01	19.9	10.0	0.16	2.1	0.88	0.02	0.01	0.05	0.17	–
AWS A5.9	<0.03	19.5–22.0	9.1–11.0	<0.75	1.0–2.5	0.65–1.00	<0.03	<0.03	–	<0.75	–

*Typical wire composition as given by material manufacturer

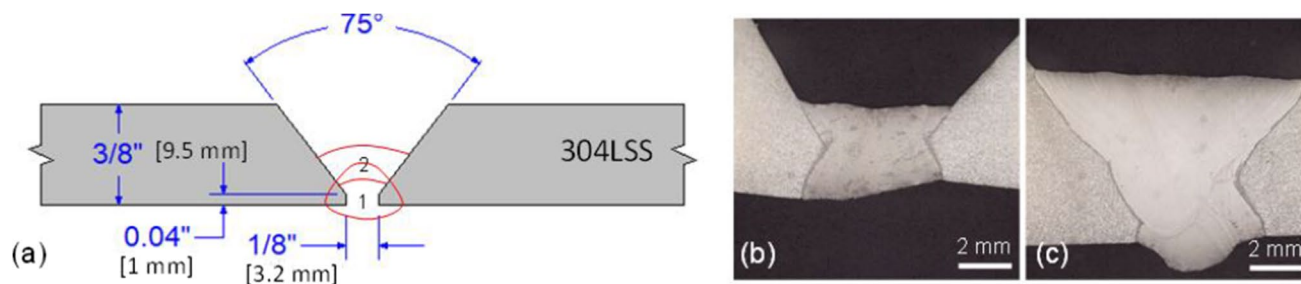


Fig. 1 a Weld joint geometry of 304L stainless steel welds, and etched cross sections from b SC-GMAW root pass-only section and c from root with additional GMAW-P hot pass section

Table 2 Overview of test welds made for this study

Weld	Type of backing gas	Wire (\varnothing 0.9 mm)
#1	None	ER308L
#2	None	ER308LSi
#3	100% Ar	ER308L
#4	100% Ar	ER308LSi
#5	95% Ar/5% O ₂	ER308L
#6	95% Ar/5% O ₂	ER308LSi

pass-only section, and the SC-GMAW root with additional GMAW-P hot pass section. Cross sections were prepared using standard metallographic procedures and electrochemically etched with 10% oxalic acid. Light optical microscopy (LOM) was used for the observation of fusion zone and heat-affected zone microstructures. Weld metal ferrite content was determined by magnetic measurements using a Fischer Feritscope FMP30. Feritscope measurements were obtained as an average of ten readings on each weld cross sections. Due to the size of the probe, measurements on the SC-GMAW root pass plus GMAW-P hot pass weld sections incorporated both weld beads. One-inch weld sections were extracted for imaging and analysis of the heat tint oxidation in the heat-affected zone on the weld backside using the scanning electron microscope (SEM). The sample surface was rinsed with ethanol prior to imaging at 20 kV and 6.4 nA. Measurements of oxide size were performed on SEM images using ImageJ software. Electron diffraction spectroscopy (EDS) was used to obtain compositional measurements from the heat tint oxidation as a function of distance from the fusion line into the heat-affected zone. SEM imaging and EDS analysis was performed on the GMAW ER308LSi welds with no-backing gas (NBG) and with 100% Ar backing gas only.

2.3 Raman spectroscopy

Raman spectroscopy was performed to determine the chemical compounds present on the heat-tinted surface in the

heat-affected zone of the weld backside. Qualitative Raman spectra were obtained for the GMAW ER308LSi welds with no-backing gas (NBG) and with 100% Ar backing gas only. Raman spectroscopy was performed using a Renishaw inVia Raman microscope with 780 nm laser excitation and a power of about 10 mW at the sample. Prior to Raman analysis, the sample surface was rinsed with deionized water followed by an ethanol rinse. Five measurements were performed on each sample with a sampling time of 60 s. An effort was made to avoid deep scratches on the sample surface.

2.4 Electrochemical corrosion testing

The objective of this study was to measure pitting corrosion resistance locally in the heat-affected zone and the back bead of the root pass that gets exposed to the corrosive environment during field service. Previous studies have proposed rather complicated cells to isolate localized regions for corrosion testing, or performed full immersion tests with masking [8, 9]. However, there are concerns of crevice corrosion in any masked immersion experiment, in particular in pitting corrosion testing of metals that are susceptible to crevice attack, such as Type 304 austenitic stainless steel [10]. The onset of crevice corrosion prior to initiation of pitting often interferes with the assessment of the critical pitting potential (E_{pit}). To avoid these issues, a simple syringe cell, first proposed by Panindre et al. [7], was utilized in this study for electrochemical corrosion testing. In this technique, the exposed area is defined by a hanging droplet (no masking required), which is approximately 0.15–0.20 cm² in size. This enables corrosion testing in a localized region on the metal surface and prevents crevice corrosion to form. Details on the syringe cell setup can be found in [7, 11]. In this study, a 50 ml capacity syringe was used with a platinum wire as a counter electrode, an Ag/AgCl reference electrode, and the weld sample as the working electrode. The syringe cell setup is shown in Fig. 2a. Testing was performed at room temperature. Ambient humidity was increased to at least 40% to minimize evaporation of the droplet during testing.

Table 3 Summary of welding parameters

Parameter	Root pass weld	Hot pass weld
Process	SC-GMAW	GMAW-P
Shielding gas	90% He/7.5% Ar/2.5% CO ₂	
Wire feed speed (in/min)	160	450
Voltage (V)	18.8–19.9	15.9–27.3
Current (A)	78.5–86.4	130.9–153.0
True energy heat input (kJ/in)	9.6–13.5	16.5–19.4
Travel speed (in/min)	7.1–9.4	12.8–15.0
Interpass temperature (°F)	75	108–133
Angle of plate in 1G position (°)	50	10

Cyclic potentiodynamic polarization (CPP) measurements based on ASTM G61 [12] were performed to determine resistance to localized (pitting) corrosion in the heat-affected zone (HAZ) and root weld metal on the backside surface of the welds. Prior to testing, the HAZ region was mechanically ground with SiC papers to 600 grit followed by an ethanol rinse and dried in hot air to expose a fresh surface. Figure 2b shows a photograph of the droplet positioned in the weld backside HAZ. Note that the photograph was taken for illustration purposes only; CPP measurements on the as-welded surface, i.e., with the heat tint oxidation present did not yield acceptable curves. After measurements on the HAZ were completed, the root bead reinforcement was ground plane to enable testing of the root weld metal (Fig. 2c). The root bead region was ground to 600 grit followed by an ethanol rinse and hot air-dried. CPP curves were recorded in a 0.1 M NaCl solution aerated at room temperature using deionized water. This is a deviation from ASTM G61, which uses 0.6 M NaCl solution. The lower strength of the solution used in this study was primarily to increase the sensitivity of the measurements since lower Cl⁻ concentrations can increase the range at which the pitting

potential (E_{pit}) and repassivation potential (E_{rp}) start. Theoretically, this would help show small differences between weld samples as opposed to the harsh attack from more concentrated solutions. CPP curves were obtained using a potentiostat (Gamry Instruments) to step up the potential at a scan rate of 1.0 mV/s from -0.2 V below the open-circuit potential (E_{OC}). The potential scan direction was reversed at a current density of 0.1 mA/cm² and the potential was stepped down to -0.2 V below the E_{OC} . ASTM G61 uses a much slower forward and reverse scan rate of 0.167 mV/s. The higher scan rate in this study was used to help offset droplet evaporation, which is a major concern in syringe cell testing. For the same reason, samples were exposed to the open-circuit potential for only 80–100 s prior to the start of the CPP measurements. At least four, and up to ten CPP curves were obtained from different positions along the backside HAZ and from the root bead weld metal for each weld. A root pass-only and a filled GTAW weld using ER308L filler wire and 100% Argon backing gas were tested as a reference. The critical pitting potential (E_{pit}) was determined from the breakdown potential. The repassivation potential (E_{rp}) was determined once a full positive hysteresis

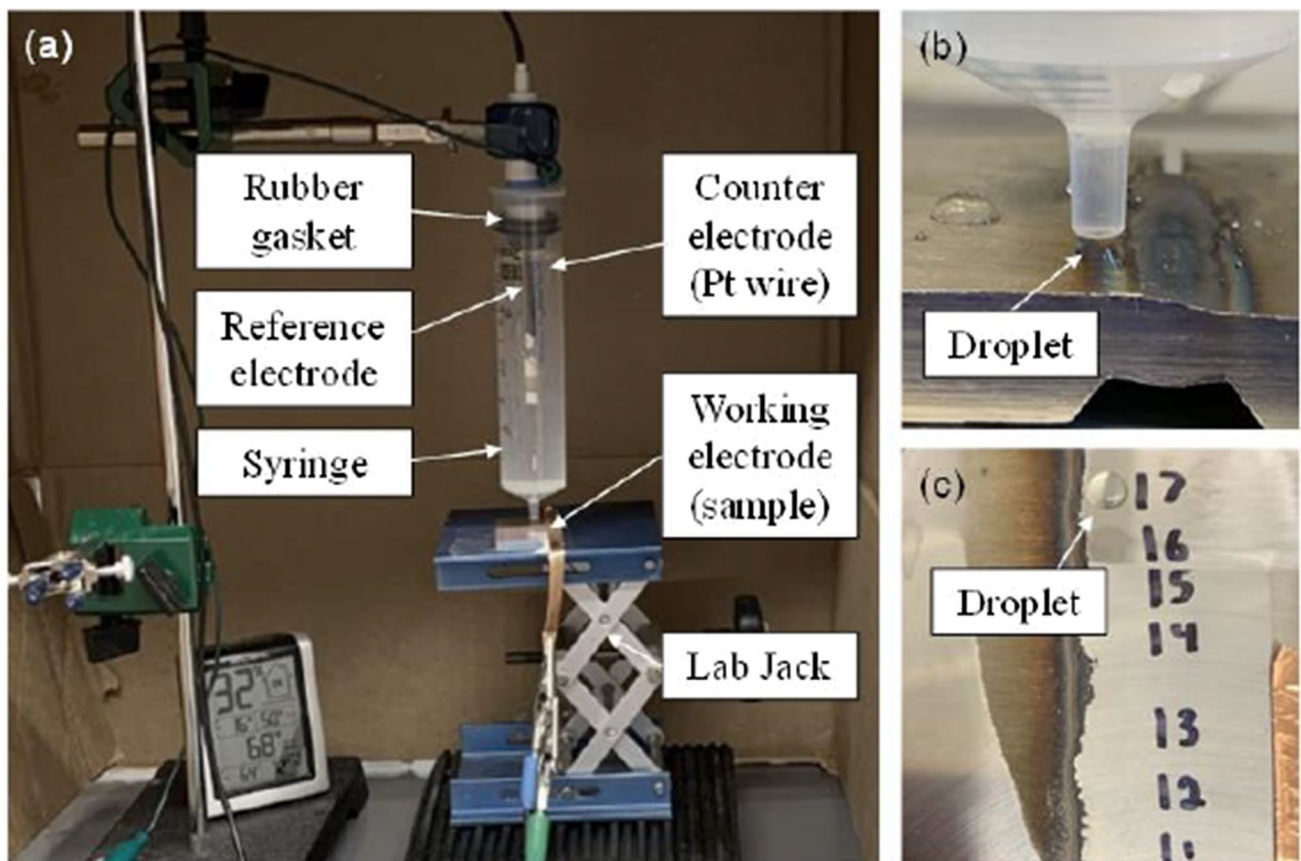


Fig. 2 **a** Syringe cell setup for electrochemical corrosion testing; **b** droplet placed in backside heat-affected zone (HAZ); and **c** droplet placed in root weld metal (WM). Note that the HAZ was polished to 600 grit prior to corrosion testing, contrary to what is shown in the photograph

was completed. Light optical microscopy was performed after testing to examine the extent of pitting on the sample surface. Statistical analysis (ANOVA) in Minitab Software was utilized to analyze the results for statistically significant differences in pitting resistance between the welds as a function of type of backing gas, filler wire, and welding process.

3 Results and discussion

3.1 Weld root appearance

A simple eye test following visual guidance provided in AWS D18.1/D18.1 M [13] was used to determine the degree of discoloration in the heat-affected zone (HAZ) of the GMAW ER308LSi and ER308L welds. Figure 3 illustrates the backbead appearance of the GMAW ER308LSi welds as a function of type of backing gas used (NBG, 100% Ar, and 95% Ar/5% O₂). All welds appeared similar in their heat tint oxidation. The discoloration from the fusion boundary outward was black, then yellow, blue, orange, and yellow again. The width of the heat tint on the weld backbead (in particular the black and blue colored regions) was larger for the SC-GMAW root plus additional GMAW-P hot pass sections (bottom images in Fig. 3) as compared to the SC-GMAW root pass-only weld sections (top) due to the additional thermal cycle experienced by the root pass. The 100% Ar backing gas welds showed the least amount of oxidation on the weld backside surface, followed by the 95% Ar/5% O₂ backing gas weld. Significantly more root bead surface oxidation was observed on the no-backing gas (NBG) welds (Fig. 3a, d). In addition, the partially scaled surface of the NBG root pass lacked the prominent “stacked-dime” appearance that is typical for short-arc GMAW processes and was

observed for the 100% Ar and 95% Ar/5% O₂ backing gas welds. It is hypothesized that chromium and other oxygen-affine elements combine with oxygen to form a viscous, slag-like covering on the molten pool, which interferes with the formation of a uniformly spaced freeze line pattern in the NBG welds.

3.2 Root weld metal ferrite content

Figure 4A shows the average ferrite content and corresponding standard deviation for the GMAW ER308LSi and ER308L welds as a function of type of backing gas used (NBG, 95% Ar/5% O₂ and 100% Ar). The ferrite content is generally similar across all weld metals, roughly between 8 and 12 FN. Comparing the SC-GMAW root pass-only welds (blue bars in Fig. 4a), the average ferrite content in the no-backing gas (NBG) welds is slightly lower as compared to the argon backing gas welds. However, taking into account the standard deviation for each weld metal, this difference is most apparent for the GMAW ER308LSi welds. The addition of a GMAW-P hot pass (grey bars in Fig. 4a) resulted in a reduction in average ferrite content for the argon backing gas welds, while the ferrite content in the NBG welds remained the same or increased slightly. Representative microstructures from the GMAW ER308LSi NBG and 100% Ar backing gas weld are shown in Fig. 4b and c, respectively. All weld metals exhibited primarily skeletal ferrite with localized areas of lathy ferrite dispersed throughout. These ferrite morphologies result from FA solidification mode, i.e., solidification initiates as ferrite and austenite forms at the end of solidification. Upon solid-state cooling, the ferrite partially transforms into austenite. The ferrite morphology and residual ferrite content at room temperature is dependent on the weld metal composition and the cooling rate of

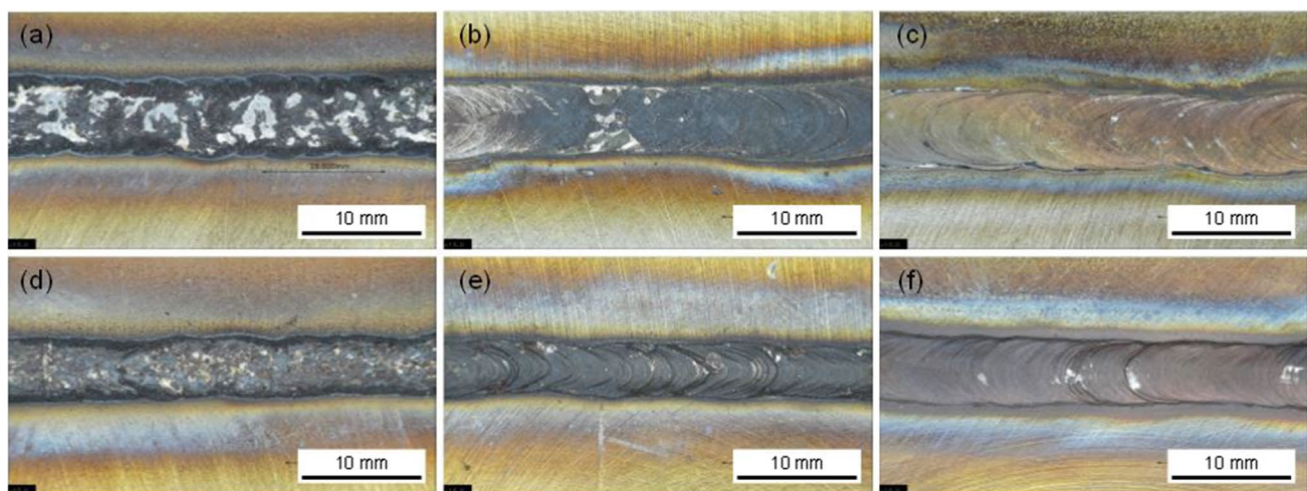
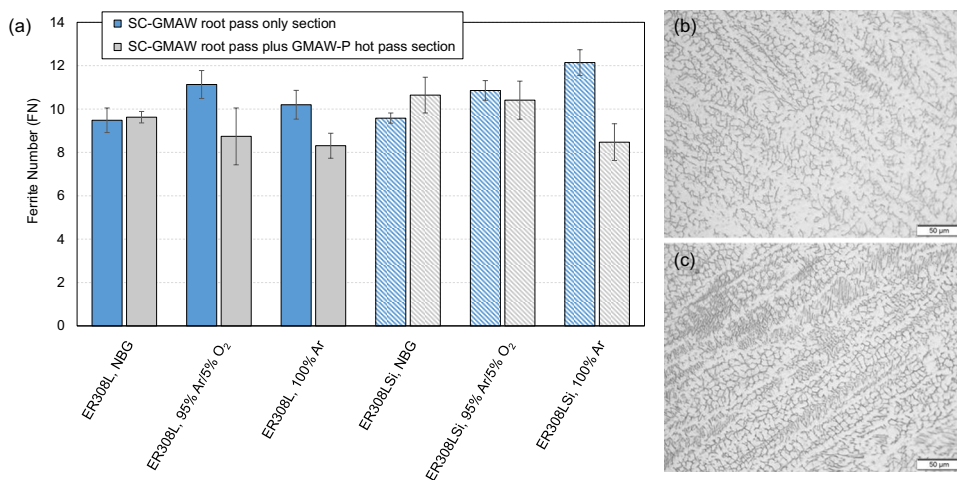


Fig. 3 Weld root appearance of GMAW ER308LSi welds from SC-GMAW root pass-only sections (top) and root plus additional GMAW-P hot pass sections (bottom): **a, d** no-backing gas (NBG) welds, **b, e** 95% Ar/ 5% O₂ backing gas welds, and **c, f** 100% Ar backing gas welds

Fig. 4 a Weld metal ferrite content (FN) measured with Feritscope on cross sections of GMAW ER308LSi and ER308L welds. Error bars show standard deviation. Etched weld microstructures of **b** GMAW ER308LSi no-backing gas (NBG) weld, and **c** GMAW ER308LSi with pure argon backing weld (both from root pass-only section)



the weld [14]. Open-gap root pass welding without backing gas results in the formation of an oxide slag covering the molten metal (as seen in Fig. 3). This may result in a loss of ferrite-promoting elements (most notably chromium) from the weld metal and explain the observed slightly lower ferrite content in the NBG root pass welds as compared to the argon backing gas weld. However, this will need further detailed compositional analysis in the weld metal that was outside of the scope of this work. The reduction in weld metal ferrite content in the argon backing gas welds after the addition of a GMAW-P hot pass is attributed to the high heat input of the hot pass weld (Table 3) and the associated slower cooling of the weld metal. The root pass gets reheated and partially remelted and the lower cooling rate allows for a more solid-state ferrite-to-austenite transformation. It is not clear why this effect is not observed for the NBG welds. It is noted however that due to the size of the probe, measurements on the SC-GMAW root pass plus GMAW-P hot pass weld sections incorporated both weld beads, which might obscure the results.

3.3 Pitting corrosion resistance

Figure 5 shows cyclic potentiodynamic polarization (CPP) curves obtained in 0.1 M NaCl solution in the backside heat-affected zone (HAZ) and the root weld metal (WM) of the GMAW ER308LSi welds. The curves shown were obtained on the SC-GMAW root plus additional GMAW-P hot pass weld sections. CPP curves from a filled GTAW with argon backing gas are shown as a reference. All curves exhibit a positive hysteresis loop (i.e., reverse scan current was higher than the forward scan current) associated with pitting corrosion. CPP curves obtained from the root weld metal (Fig. 5b) exhibit a clearly defined passive current density, while curves from the backside HAZ show a wider passive range. From the CPP curves, the pitting potential (E_{pit}), above which stable pits initiate rapidly, and the repassivation

potential (E_{rp}), below which stable pits cease to grow, were determined. The pitting potential is characterized by a sharp increase in current density as the potential is stepped up during the test. As the potential scan direction is reversed, repassivation occurs towards the repassivation potential, which is taken when the hysteresis loop is complete and the current density reaches the passive current density.

Table 4 and Table 5 summarize the average values and corresponding standard deviations for pitting potential and repassivation potential as determined from the CPP curves for all tested welds. Figure 6 compares the pitting and repassivation potentials obtained in the backside HAZ of the GMAW ER308LSi and ER308L welds. Data is shown for the root plus additional hot pass weld sections. Results from a filled GTAW with argon backing are shown as a reference. The pitting potential of the backside HAZ of the no-backing gas (NBG) welds was slightly lower as compared to the GMAW argon backing gas and the GTAW reference welds. The repassivation potential of the backside HAZ of the NBG welds was comparable to the GMAW argon backing gas and the GTAW reference weld. Statistical analysis (ANOVA) indicated that there was no statistically significant difference in the corresponding means (see Table I-S and Table II-S in supplementary material).

Figure 7 compares the pitting and repassivation potentials obtained in the root weld metal of the GMAW ER308LSi and ER308L welds. Data is shown for the root plus additional hot pass weld sections. Results from a filled GTAW with argon backing are shown as a reference. The pitting potential of the root weld metal of the NBG welds was slightly lower as compared to the GMAW argon backing gas, but comparable to the GTAW reference weld. The repassivation potential of the root pass weld metal of the NBG welds was comparable to the GMAW argon backing gas and the GTAW reference welds. There was no statistically significant difference in the corresponding means (see Table III-S and Table IV-S in supplementary material). The pitting and

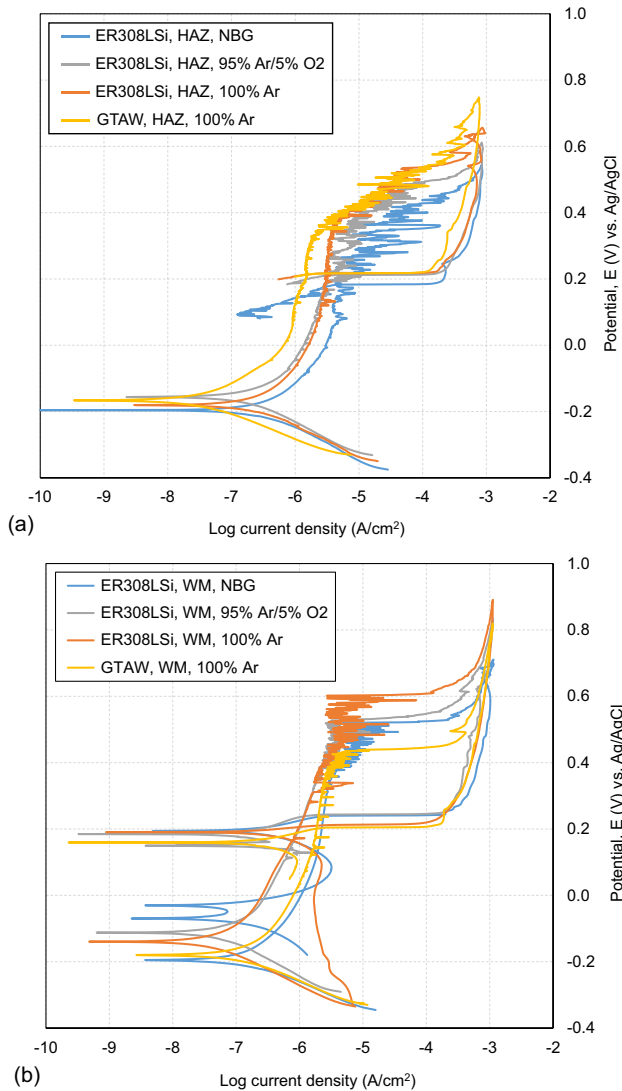


Fig. 5 Representative cyclic potentiodynamic polarization (CPP) curves for GMAW ER308LSi welds obtained in 0.1 M NaCl solution at room temperature in **a** the backside heat-affected zone (HAZ), and **b** the root weld metal (WM) comparing no-backing gas (NBG) welds to welds with 100% Ar and 95%Ar/5% O₂ backing gases. CPP curves shown were recorded on the SC-GMAW root plus additional GMAW-P hot pass weld sections. A filled GTAW weld with 100% Ar backing gas is also shown and was tested as reference

repassivation potentials of the root weld metal were comparable between the ER308LSi and ER308L welds. Silicon has been shown to increase the resistance to pit initiation, resulting in slower corrosion rates [15]. This does not appear to play a role under the environmental conditions tested in this study. Overall, the pitting and repassivation potentials obtained for the root weld metals were either comparable or slightly lower as compared to what was obtained for the corresponding weld backside HAZ (comparing Figs. 6 and 7, and Tables 4 and 5). This may explain the observation of pitting corrosion in the root bead in previous immersion

tests according to ASTM G48 Method A [6] performed on similar welds [5].

In general, the pitting potential is more sensitive to microstructure and surface conditions than the repassivation potential. However, the pitting potential is not a conservative measure for long-term performance prediction as localized corrosion can occur at potentials lower than the pitting potential. The repassivation potential has been shown to be a better indicator of long-term pitting performance [16, 17]. From this perspective, it appears that the NBG welds have a similar performance to the argon backing gas welds and the GTAW reference welds. This echoes previous results from standard immersion testing that had shown no significant difference in corrosion weight loss between GMAW NBG welds and reference GTAW welds with argon backing [5]. It should be noted that the as-welded backside root surface (i.e., with the heat tint oxidation present) was immersed in the prior work, while in the present study, the HAZ and root weld metal had to be ground to 600 grit prior to corrosion testing (as described in Sect. 2.4). For this reason, additional characterization of the heat tint oxidation in the HAZ was performed on the GMAW NBG welds and compared to results obtained from the pure argon backing gas weld as described in the following two sections.

3.4 Heat tint oxidation analysis

SEM images of oxides in the backside HAZ of the GMAW ER308LSi weld using no-backing gas (NBG) versus 100% Argon backing gas are shown in Fig. 8a–f. Images were taken as a function of distance from the fusion boundary out into the heat tint oxidation of the HAZ. Oxide size was measured using ImageJ software. Oxides were significantly larger right at the fusion boundary in the NBG weld (~0.6 μm) as compared to the 100% Argon backing gas weld (~0.3 μm). At a 1 mm distance from the fusion boundary and beyond, individual oxide particles in both welds were too small to measure in the SEM (<0.1 μm), and seemed generally comparable in size.

EDS point analysis as a function of distance from the fusion boundary on the heat-tinted sample surface of both welds is shown in Fig. 8g and Fig. 8h, respectively. Significantly more oxygen was picked up in the NBG weld as compared to the 100% Ar backing gas weld. EDS is a semi-quantitative measuring technique; in particular, quantification of oxygen is not possible. Nonetheless, these results in conjunction with the larger measured oxide size indicate a thicker heat tint oxidation layer in the HAZ of the NBG welds as compared to the pure argon backing gas welds. The rapid decrease in oxygen content and oxide size at increasing distance from the fusion boundary is indicative of a decreasing thickness of the heat tint oxidation independent of the type of backing gas used.

Table 4 Results from cyclic potentiodynamic polarization (CPP) measurements for backside heat-affected zone (HAZ) and root weld metal (WM) of GMAW ER308LSi and ER308L welds: data obtained

from the root plus additional hot pass section. Average values with standard deviation are given

Welding process	Filler wire	Type of backing gas	Test location	Pitting potential (E_{pit}) in $mV_{Ag/AgCl}$	Repassivation potential (E_{rp}) in $mV_{Ag/AgCl}$
GMAW	ER308LSi	None	HAZ	466 ± 33	181 ± 56
		95% Ar/5% O ₂		526 ± 19	244 ± 30
		100% Ar		525 ± 30	206 ± 18
GMAW	ER308L	None	HAZ	455 ± 17	201 ± 28
		95% Ar/5% O ₂		568 ± 13	255 ± 25
		100% Ar		568 ± 38	230 ± 41
GTAW*	ER308L	100% Ar	HAZ	534 ± 74	245 ± 99
GMAW	ER308LSi	None	WM	475 ± 40	180 ± 58
		95% Ar/5% O ₂		612 ± 82	179 ± 55
		100% Ar		573 ± 69	238 ± 58
GMAW	ER308L	None	WM	477 ± 50	194 ± 20
		95% Ar/5% O ₂		545 ± 31	232 ± 20
		100% Ar		528 ± 24	186 ± 20
GTAW*	ER308L	100% Ar	WM	451 ± 14	182 ± 13

*Standard reference weld with 100% Ar backing gas was completely filled

Table 5 Results from cyclic potentiodynamic polarization (CPP) measurements for backside heat-affected zone (HAZ) and root weld metal (WM) of GMAW ER308LSi and ER308L welds: data obtained

from the root pass–only section. Average values with standard deviation are given

Welding process	Filler wire	Type of backing gas	Test location	Pitting potential (E_{pit}) in $mV_{Ag/AgCl}$	Repassivation potential (E_{rp}) in $mV_{Ag/AgCl}$
GMAW	ER308LSi	None	HAZ	474 ± 25	201 ± 28
		95% Ar/5% O ₂		498 ± 17	197 ± 84
		100% Ar		519 ± 24	214 ± 28
GMAW	ER308L	None	HAZ	461 ± 27	196 ± 15
		95% Ar/5% O ₂		596 ± 11	295 ± 36
		100% Ar		556 ± 10	231 ± 33
GTAW	ER308L	100% Ar	HAZ	550 ± 27	167 ± 42
GMAW	ER308LSi	None	WM	503 ± 94	180 ± 47
		95% Ar/5% O ₂		557 ± 29	216 ± 63
		100% Ar		637 ± 70	268 ± 66
GMAW	ER308L	None	WM	484 ± 39	204 ± 21
		95% Ar/5% O ₂		604 ± 123	182 ± 23
		100% Ar		579 ± 74	208 ± 8
GTAW	ER308L	100% Ar	WM	483 ± 39	196 ± 9

This was also reported by Ling et al. [18] who performed GTAW without back purging on the 304L base plate and analyzed the oxidation on the backside heat-affected zone. The oxide size and oxygen content of the oxide film were the largest and closest to the fusion boundary, similar to what has been observed in the present work. The higher degree of oxidation was attributed to the peak temperatures being highest at the fusion boundary [18].

No results from reference (pure argon backing) welds were presented.

Ling et al. [18] also reported the type of oxides to vary as a function of distance from the fusion boundary. Fe-rich oxides (Fe₂O₃ and Fe₃O₄) were observed in regions closest to the fusion boundary. At about 2 mm distance, Cr-rich oxides (Cr₂O₃) were identified, roughly corresponding to the blue region in the heat-tinted heat-affected zone. Further

Fig. 6 Pitting potential (E_{pit}) and repassivation potential (E_{rp}) values determined from CPP curves for the backside heat-affected zone (HAZ) of the GMAW ER308LSi and ER308L welds. Data is shown for the root plus additional hot pass welds. Error bars indicate minimum and maximum values measured. The asterisk shows data obtained from a root pass-only (blue bar) and a filled (grey bar) GTAW with argon backing is given as a reference

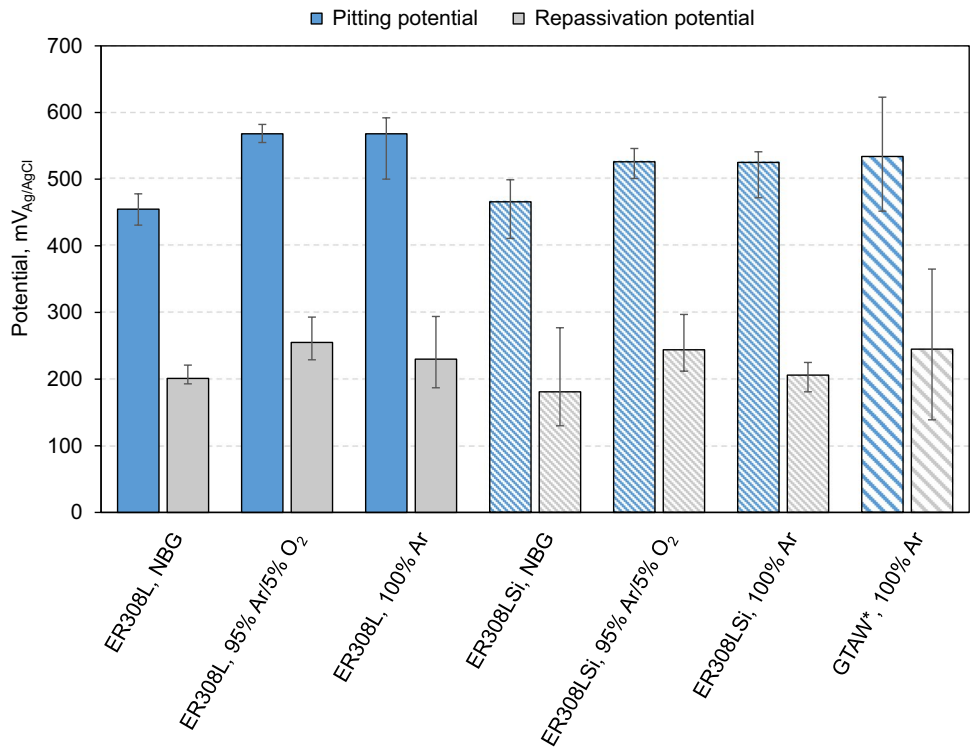
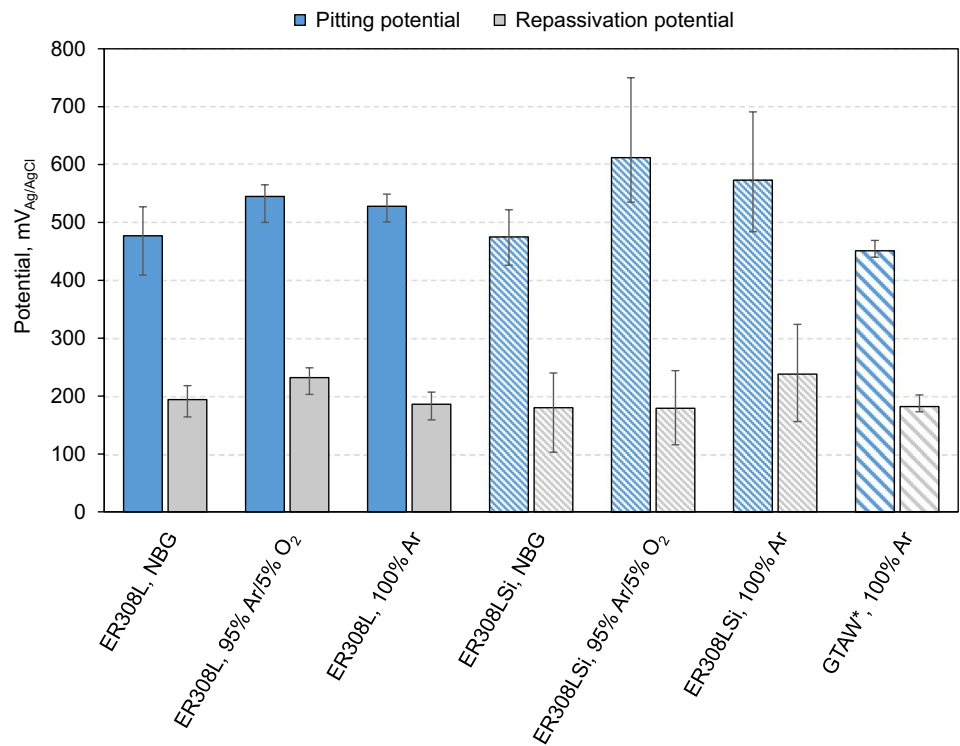


Fig. 7 Pitting potential (E_{pit}) and repassivation potential (E_{rp}) values determined from CPP curves for the root pass weld metal (WM) of the GMAW ER308LSi and ER308L welds. Data is shown for the root pass additional hot pass welds. Error bars indicate minimum and maximum values measured. The asterisk shows data obtained from a root pass-only (blue bar) and a filled (grey bar) GTAW with argon backing is given as a reference



out, Fe-rich and Fe–Cr-rich oxides (Fe_3O_4 , $FeCr_2O_4$) dominated the oxide film composition. In the present work, Raman spectra were obtained only from the region immediately adjacent to the fusion boundary. Five scans were obtained from the backside HAZ of the GMAW ER308LSi

weld using no-backing gas (NBG) and 100% Argon backing gas (Fig. 9). The observed compounds in both welds were very similar and identified as predominantly Fe-rich oxides, particularly Fe_2O_3 and Fe_3O_4 , in good agreement with previous work [18–20].

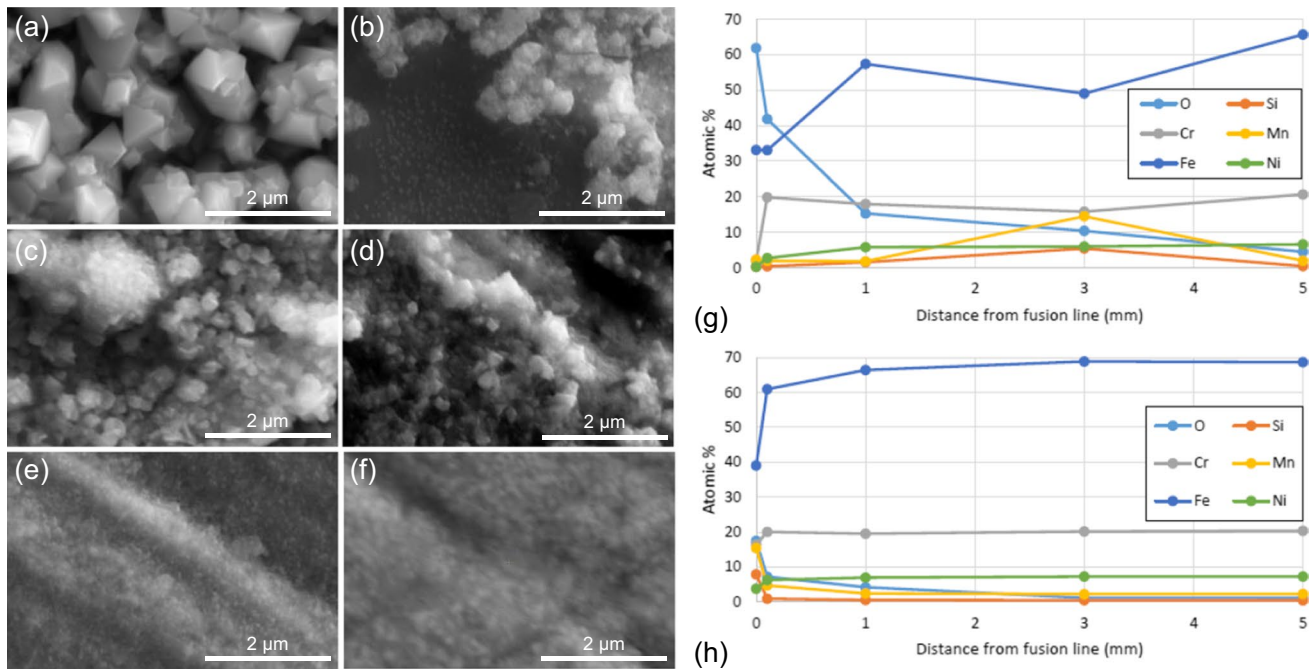


Fig. 8 SEM imaging of heat tint oxidation in the heat-affected zone of the GMAW ER308LSi welds with **a, c, e** no-backing gas (NBG), and **b, d, f** 100% Ar backing gas at 0 mm (**a, b**), 0.1 mm (**c, d**), and 1 mm (**e, f**) distance from the fusion line. Results from EDS point

analysis on heat tint oxidation as a function of distance from the fusion line: **g** no-backing gas (NBG), and **f** 100% Ar backing gas weld

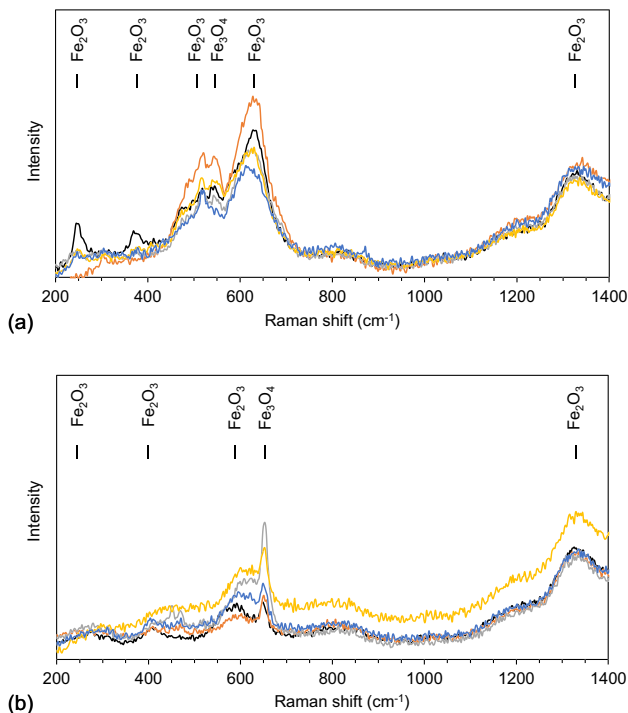


Fig. 9 Raman spectra from heat tint oxidation in the heat-affected zone of the GMAW ER308LSi weld with **a** no-backing gas (NBG), and **b** 100% Ar backing gas

4 Conclusions

This study indicates that open-gap root pass welding of austenitic stainless steel using waveform-controlled gas metal arc welding (GMAW) shows promise as a viable welding technique, competitive with GMAW and GTAW with backing gas. The obtained results on weld root appearance, weld metal microstructure, and corrosion performance can be summarized as follows:

1. The GMAW no-backing gas welds (NBG) appeared similar to the argon backing gas welds in terms of heat tint oxidation and discoloration in the backside heat-affected zone (HAZ). The NBG welds exhibited significantly more soot and oxide islands on the root bead weld metal as compared to the argon backing gas welds. In addition, the NBG root pass lacked the typical “stacked-dime” appearance.
2. The weld metal ferrite content was similar for the GMAW NBG and argon backing gas welds. The NBG welds showed a slightly lower average ferrite content in the root pass—only welds as compared to the argon backing gas welds.
3. Cyclic potentiodynamic polarization (CPP) measurements in 0.1 M NaCl solution using a syringe cell arrangement enabled the characterization of pitting corrosion performance locally in the backside HAZ and

root weld metal. However, the sample surface had to be ground to 600 grit prior to testing; CPP measurements on the as-welded surface, i.e., with the heat tint oxidation present did not yield acceptable curves.

4. The NBG welds exhibited a slightly lower pitting potential in the backside HAZ and root weld metal as compared to the argon backing gas welds and the reference GTAW with argon backing. However, the repassivation potential of the NBG welds was comparable to the argon backing welds and the reference GTAW with argon backing. The latter indicates that the NBG welds have a similar pitting corrosion performance to the argon backing gas welds and the GTAW reference welds. This is in good agreement to previous results from immersion testing that had shown comparable corrosion weight loss between GMAW NBG welds and GTAW reference welds with argon backing. Further longer-term testing of weldments under immersion conditions will be necessary to fully characterize the corrosion resistance of the NBG welds in different corrosive environments.
5. Oxide particle size in the heat tint oxidation layer on the backside HAZ of the NBG welds was larger as compared to the argon backing gas welds. This difference was most pronounced very close (< 1 mm) to the fusion boundary. Compositional analysis (EDS) picked up considerably more oxygen on the heat-tinted sample surface of the NBG welds as compared to the argon backing gas welds. This indicates a larger thickness of the heat tint oxidation layer in the HAZ of the NBG welds as compared to the pure argon backing gas welds. The observed compounds in the heat tint oxidation close to the fusion line were very similar, being primarily Fe-rich oxides, in particular Fe_2O_3 and Fe_3O_4 . At an increasing distance from the fusion line, both oxide size and oxygen content are comparable between NBG and argon backing gas welds.

Supplementary Information The online version contains supplementary material available at <https://doi.org/10.1007/s40194-022-01442-x>.

Acknowledgements The authors would like to thank Jorge Penso (Shell Global Solutions Inc.), who provided insight and expertise that was of great value to this research. The authors would also like to acknowledge the valuable contributions of Michael Barrett and Griffin Goldenbagen of the Lincoln Electric Company for conducting all the welding presented in this manuscript. In addition, undergraduate research student Frederico Aponte is acknowledged for his support in sample preparation. Electron microscopy was performed at the Center for Electron Microscopy and Analysis (CEMAS) at The Ohio State University. Corrosion testing was performed at the Fontana Corrosion Center at The Ohio State University.

Funding Financial support was provided by the Manufacturing & Materials Joining Innovation Center (Ma²JIC), made possible through

an award (2052747) from the National Science Foundation Industry University Cooperative Research Center Program (IUCRC) and an Research Experience for Undergraduate Supplement.

Declarations

Conflict of interest The authors declare no competing interests.

References

1. Chiluvuri SK, Bliss K, Penso J (2019) Evaluation of welding techniques for stainless steels piping without use of backing gas. In: ASME 2019 Pressure Vessels and Piping Conference, vol 6B. Materials and Fabrication, San Antonio, TX, pp PVP2019-93359. <https://doi.org/10.1115/PVP2019-93359>
2. Messer B, Lawrence G, Oprea V, Patrick C, Phillips T (2002) Welding stainless steel piping with no backing gas. *Weld J* 81:32–34
3. Messer B, Seitz S, Patrick C, Armstrong K (2005) A novel technological assessment for welding heavy wall stainless steel. In: ASME 2005 pressure vessels and piping conference, vol 6. Materials and Fabrication, Denver, CO, PVP 2005, pp 527–533. <https://doi.org/10.1115/PVP2005-71412>
4. Patrick CW, Ferguson TE (2004) P91 pipe welding breakthrough. In Proceedings from the Fourth International Conference on Advances in Materials Technology for Fossil Power Plants, Hilton Head Island, SC, USA, pp. 803–836
5. Rajan V, Narayanan B, Barrett M, Beardsley K (2020) Stainless steel pipe welding with no backing gas. In: ASME 2020 pressure vessels and piping conference, vol 6. Materials and Fabrication, Minneapolis, MN, pp PVP2020-21799. <https://doi.org/10.1115/PVP2020-21799>
6. ASTM G48–11 (2020) Standard test methods for pitting and crevice corrosion resistance of stainless steels and related alloys by use of ferric chloride solution. ASTM International, 2020
7. Panindre AM, Chang KH, Weirich T, Frankel GS (2018) Technical note: syringe cell for electrochemical testing. *Corros* 74:847–850. <https://doi.org/10.5006/2847>
8. Ovarfort R (1988) New electrochemical cell for pitting corrosion testing. *Corros Sci* 28:135–140. [https://doi.org/10.1016/0010-938X\(88\)90090-X](https://doi.org/10.1016/0010-938X(88)90090-X)
9. Lohrengel MM, Moehring A, Pilaski M (2000) Electrochemical surface analysis with the scanning droplet cell. *Fresenius' J Anal Chem* 367:334–339. <https://doi.org/10.1007/s002160000402>
10. Stockert L, Hunkeler F, Bohni H (1985) Technical note: a crevice-free measurement technique to determine reproducible pitting potentials. *Corros* 41:676–677. <https://doi.org/10.5006/1.3583002>
11. Panindre AM, Frankel GS (2021) Technical note: electrochemical testing for pitting corrosion above ambient temperatures using the syringe cell. *Corros* 77:1025–1028. <https://doi.org/10.5006/3854>
12. ASTM G61–86 (2018) Standard test method for conducting cyclic potentiodynamic polarization measurements for localized corrosion susceptibility of iron-, nickel-, or cobalt-based alloys. ASTM International, 2018
13. AWS D18.1/D18.1M:2020 Specification for welding of austenitic stainless steel tube and pipe systems in sanitary (hygienic) applications. American Welding Society, 2020
14. Brooks JA, Thompson AW (1991) Microstructural development and solidification cracking susceptibility of austenitic stainless steel welds. *Int Mater Rev* 36(1):16–44

15. Wilde BE (1986) The influence of silicon on the pitting corrosion resistance of an 18Cr-8Ni stainless steel. *Corros* 42:147–151. <https://doi.org/10.5006/1.3584894>
16. Sridhar N, Cragolino GA (1993) Applicability of repassivation potential for long-term prediction of localized corrosion of alloy 825 and Type 316L stainless steel. *Corros* 49:885–894. <https://doi.org/10.5006/1.3316014>
17. Dunn DS, Cragolino GA, Sridhar N (2000) An electrochemical approach to predicting long-term localized corrosion of corrosion-resistant high-level waste container materials. *Corros* 56:90–104. <https://doi.org/10.5006/1.3280526>
18. Ling LG, Liu TG, Lu YH, Guo PL (2019) Investigation of the oxides film on 304L base metal produced during welding process without inert gas shielding. *Appl Surf Sci* 465:780–786. <https://doi.org/10.1016/j.apsusc.2018.09.189>
19. Ling LG, Liu TG, Lu YH (2018) Investigation of the oxide film on 308L weld surface produced during welding process. *Mater Charact* 146:113–120. <https://doi.org/10.1016/j.matchar.2018.09.011>
20. Kim J, Choi KJ, Bahn CB, Kim JH (2014) In situ Raman spectroscopic analysis of surface oxide films on Ni-base alloy/low alloy steel dissimilar metal weld interfaces in high-temperature water. *J Nucl Mater* 449:181–187. <https://doi.org/10.1016/j.jnucmat.2014.03.038>

Publisher's note Springer Nature remains neutral with regard to jurisdictional claims in published maps and institutional affiliations.

Springer Nature or its licensor (e.g. a society or other partner) holds exclusive rights to this article under a publishing agreement with the author(s) or other rightsholder(s); author self-archiving of the accepted manuscript version of this article is solely governed by the terms of such publishing agreement and applicable law.